





Article

Bimodal-Structured 0.9KNbO₃-0.1BaTiO₃ Solid Solutions with Highly Enhanced Electrocaloric Effect at Room Temperature

Hongfang Zhang ^{1,*}, Liqiang Liu ², Ju Gao ^{3,*}, K. W. Kwok ⁴, Sheng-Guo Lu ^{5,*} , Ling-Bing Kong ⁶ , BiaoLin Peng ⁷ and Fang Hou ¹

¹ School of Physical Science and Technology, Suzhou University of Science and Technology, Suzhou 215009, China

² Center for Advanced Ceramics, School of Materials Science and Engineering, Anhui Polytechnic University, Wuhu 241000, China

³ School of Optoelectronic Engineering, Zaozhuang University, Zaozhuang 277160, China

⁴ Department of Applied Physics, The Hong Kong Polytechnic University, Hung Hom, Kowloon, Hong Kong

⁵ Guangdong Provincial Research Center on Smart Materials and Energy Conversion Devices, Guangdong Provincial Key Laboratory of Functional Soft Condensed Matter, School of Materials and Energy, Guangdong University of Technology, Guangzhou 510006, China

⁶ College of New Materials and New Energies, Shenzhen Technology University, Shenzhen 518118, China

⁷ School of Advanced Materials and Nanotechnology, Xidian University, Xi'an 710126, China

* Correspondence: constance_zhanghf@126.com (H.Z.); jugao@hku.hk (J.G.); sglu@gdut.edu.cn (S.-G.L.)

Abstract: 0.9KNbO₃-0.1BaTiO₃ ceramics, with a bimodal grain size distribution and typical tetragonal perovskite structure at room temperature, were prepared by using an induced abnormal grain growth (IAGG) method at a relatively low sintering temperature. In this bimodal grain size distribution structure, the extra-large grains (~10–50 μm) were evolved from the micron-sized filler powders, and the fine grains (~0.05–0.35 μm) were derived from the sol precursor matrix. The 0.9KNbO₃-0.1BaTiO₃ ceramics exhibit relaxor-like behavior with a diffused phase transition near room temperature, as confirmed by the presence of the polar nanodomain regions revealed through high resolution transmission electron microscope analyses. A large room-temperature electrocaloric effect (ECE) was observed, with an adiabatic temperature drop (ΔT) of 1.5 K, an isothermal entropy change (ΔS) of 2.48 J·kg⁻¹·K⁻¹, and high ECE strengths of $|\Delta T/\Delta E| = 1.50 \times 10^{-6}$ K·m·V⁻¹ and $\Delta S/\Delta E = 2.48 \times 10^{-6}$ J·m·kg⁻¹·K⁻¹·V⁻¹ (directly measured at $E = 1.0$ MV·m⁻¹). These greatly enhanced ECEs demonstrate that our simple IAGG method is highly appreciated for synthesizing high-performance electrocaloric materials for efficient cooling devices.

Keywords: electrocaloric effect; abnormal grain growth; bimodal structure; grain-size distribution; polar nanodomain regions



Citation: Zhang, H.; Liu, L.; Gao, J.; Kwok, K.W.; Lu, S.-G.; Kong, L.-B.; Peng, B.; Hou, F. Bimodal-Structured 0.9KNbO₃-0.1BaTiO₃ Solid Solutions with Highly Enhanced Electrocaloric Effect at Room Temperature. *Nanomaterials* **2022**, *12*, 2674. <https://doi.org/10.3390/nano12152674>

Academic Editors: Dong-Joo Kim and Sam Lofland

Received: 18 June 2022

Accepted: 2 August 2022

Published: 4 August 2022

Publisher's Note: MDPI stays neutral with regard to jurisdictional claims in published maps and institutional affiliations.



Copyright: © 2022 by the authors. Licensee MDPI, Basel, Switzerland. This article is an open access article distributed under the terms and conditions of the Creative Commons Attribution (CC BY) license (<https://creativecommons.org/licenses/by/4.0/>).

1. Introduction

The electrocaloric (EC) effect refers to the adiabatic temperature change in a polar material at an electric field, due to the isothermal entropy change associated with the electric-field-induced change in polarization [1–3]. The EC effect of ferroelectric materials has attracted continuous attention because of the potential applications in solid-state refrigeration, which is regarded as the most promising solution for cooling microelectronic devices due to the ease of miniaturization, high efficiency and low cost. Based on these considerations, a high EC performance material should possess a large isothermal entropy change (ΔS) and hence large adiabatic temperature change (ΔT) under a reasonable electric field (E). In other words, large EC strengths (defined by $|\Delta T/\Delta E|$ and $\Delta S/\Delta E$, where parameters T , S and E are the temperature, isothermal entropy and applied electric field, respectively) are favored. Additionally, a wide working temperature range near room temperature (RT) is favored in order to develop high performance EC cooling devices [4–6]. Therefore, one critical question here is how to design and develop high-performance

dielectric materials which are capable of generating giant EC effect over a broad T -range near RT, at a relatively low electric field.

It has been well accepted that perovskite relaxor ferroelectrics with a first-order phase transitions could be suitable solid-state systems because they present large EC effects with a mild temperature dependency and low hysteresis loss [7,8]. Moreover, owing to their even higher EC effect, bulk ceramics are superior to any type of materials, which could be implemented in medium- and large-scale cooling devices with high refrigeration capacities [9]. However, although a series of ferroelectric perovskite materials have been explored in terms of enhanced EC effect, the ΔT is limited, and the largest ΔT is less than 2 K at a relatively large electric field, corresponding to $\Delta E < 50 \text{ kV}\cdot\text{cm}^{-1}$. This ΔT value does not meet the requirement of commercial applications [5].

Additionally, in analogy to the current trends in piezoelectric technology, highly appreciated EC materials should also be lead-free and in future be able to replace the lead-containing materials for environmental considerations. Among various ferroelectric perovskites, KNbO_3 and BaTiO_3 , typically environmentally friendly materials, with first-order ferroelectric transitions, have been paid much attention, due to their promisingly electrical properties [10]. KNbO_3 is a well-known ferroelectric material that exhibits the same symmetries and phase transition sequence as BaTiO_3 , with the structural phase transitions from cubic to tetragonal at a Curie temperature of T_c ($\sim 435^\circ\text{C}$), and from tetragonal to orthorhombic at $\sim 225^\circ\text{C}$ upon cooling from high temperature to room temperature [11]. Although KNbO_3 was theoretically calculated such that a large EC temperature change can be achieved near the Curie point, e.g., $\Delta T \sim 6 \text{ K}$ at $\sim 435^\circ\text{C}$, while $\Delta T \sim 1.5 \text{ K}$ at 120°C for BaTiO_3 [12], they are not desired for practical cooling device applications, due to their working temperatures being far above RT.

Usually, the isothermal entropy change of a ferroelectric material reaches a maximum around T_c , thus giving the largest EC effect. Therefore, a ferroelectric EC material is required to have a Curie temperature close to the device operation temperature, e.g., RT for most practical applications. Furthermore, the thermal hysteresis in terms of ferroelectric polarization over the phase transition region should be as weak as possible, since such a hysteresis loop represents the energy loss during the device operation [4]. Therefore, a high-quality EC system should have a Curie temperature around RT and exhibit weak thermal hysteresis.

An immediate choice to fit the above requirement is the KNbO_3 - BaTiO_3 solid solution which allows a remarkable reduction in the Curie temperature with respect to either KNbO_3 or BaTiO_3 . For example, the 0.9KNbO_3 - 0.1BaTiO_3 solid solution, denoted as KN-BT(9/1), exhibits a Curie temperature T_c of $\sim 50^\circ\text{C}$, which is very close to RT. In addition, the two distinctly different T_c of the ferroelectric components favor the formation of a diffused phase transition between the high-temperature paraelectric phase and the low-temperature ferroelectric phase, and thus a weak thermal hysteresis [11].

Nevertheless, the EC effect of KN-BT(9/1) has been rarely reported, mainly because the preparation of highly dense KN-BT(9/1) ceramics using the conventional solid-state reaction technology is still a challenge due to the large differences between the properties of the cations in KNbO_3 and BaTiO_3 . The melting temperature of KNbO_3 is also far lower than that of BaTiO_3 (1040°C vs. 1625°C). Moreover, the high volatility of potassium oxide (K_2O) at high temperature, such as 800°C , will result in non-stoichiometry and thus the formation of unwanted phases [13]. A novel sintering technique to prepare high quality KN-BT(9/1) ceramics is thus highly appreciated.

In this study, the newly developed sintering technique, the induced abnormal grain growth (IAGG) method [14], is applied to prepare KN-BT(9/1) ceramics with a novel bimodal grain size distribution in a simple and easy way. The bimodal grain size distribution structure (briefly called the bimodal structure) consists of a small fraction of large-sized grains uniformly embedded in the matrix of fine grains. The large grains are evolved from the micron-sized KN-BT(9/1) powders (filler), while the small ones are derived from the nano-sized KN-BT(9/1) powders (matrix). The highly dense and stoichiometric

KN-BT(9/1) ceramics are well sintered at a relatively low sintering temperature, and more importantly, exhibit a strong EC effect near RT at a low electric field.

2. Materials and Methods

2.1. Preparation of the Filler and Matrix Powders

Micron-sized KN-BT(9/1) filler powder was fabricated using KNbO₃ and BaTiO₃ as raw powders by using the conventional ceramic processing. The KNbO₃ powder was prepared from pure grade K₂CO₃ (99.99%, Aladdin) and Nb₂O₅ (99.95%, Alfa Aesar) powders, which were first ball-milled and calcined at 640 °C for 4 h. Then, the calcined powders were ball-milled again for 24 h. After drying at 120 °C overnight, the KNbO₃ powders were mixed thoroughly with a commercial-grade high purity nano-sized BaTiO₃ powder (D₅₀ = 50 nm, 99.9 wt.% purity, SAKAI Chemical Industry Co. Ltd., Osaka, Japan), in a molar ratio of 9:1, by ball-milling. The mixture was then calcined at 900 °C for 2 h, ball-milled again for 24 h, and dried at 120 °C overnight to produce the KN-BT(9/1) filler powder (Figure S1c).

A modified Pechini method was introduced to prepare KN-BT(9/1) sol precursor. All raw materials were weighed according to the designed composition. For Nb-sources, Nb₂O₅ powder was dissolved in hydrofluoric acid (48–51%, ACS, Alfa Aesar) at 80 °C. Then, ammonium hydroxide (28% NH₃, Alfa Aesar) was tardily added into the solution until the pH value reached 10, followed by filtering, washing and drying of the sediment at 80 °C for 10 h. Subsequently, niobium hydroxide was formed. The Nb source was then obtained by dissolving the niobium hydroxide in a citric acid (CA) solution. For preparing the metal–CA solution (metal: K and Ba), K₂CO₃ and BaCO₃ (99.95%, Aladdin) were dissolved directly in a CA solution. For the Ti–CA solution, tetrabutyltitanate (C₁₆H₃₆O₄Ti, 96%, Alfa Aesar) with the CA solution was heated to 80 °C until the solution became transparent. Finally, all the metal sources were mixed, with a molar ratio of CA:EG (ethylene glycol) to be 1/4 and pH value to be 10. KN-BT(9/1) precursor solution was obtained by stirring the solution at 80 °C for 2 h. The precipitant was dried at 120 °C for 24 h and then calcined at 900 °C for 2 h as a matrix powder. The detailed synthesis routes are schematically shown in Figure S1c.

2.2. Preparation of Bimodal Structured KN-BT(9/1) Ceramics

The IAGG method is schematically shown in Figure S1c. The micron-sized KN-BT(9/1) filler powder and the nano-sized KN-BT(9/1) matrix powder were first mixed thoroughly by ball balling in ethanol for 4 h. After drying at 120 °C, the mixture was then uniaxially pressed into green pellets with a diameter of 10 mm and a thickness of about 1 mm. Finally, the green pellets were sintered at 1000–1050 °C for 2 h in air with a heating rate of 2 °C·min^{−1}. For comparison, the filler powder and the matrix powder were also used separately to prepare KN-BT(9/1) ceramics by similar procedures. All the samples were cooled by natural cooling in the furnace.

2.3. Characterization

2.3.1. Microstructure and Morphology

Crystal structures were examined using X-ray diffraction (XRD, D8 ADVANCE, Bruker AXS Corporation, Karlsruhe, Germany) with CuK_{α1} radiation (1.5418 Å, 40 kV, 40 mA) from 2 theta (degree) = 15 to 70° at a scan step of 0.02° per second at room temperature. The Rietveld refinement of XRD pattern was carried out using the GSAS-EXPGUI software package (General Structure Analysis System, A.C. Larson and R.B. Von Dreele, Los Alamos National Laboratory Report LAUR 86-748 (2004); B.H. Toby, EXPGUI, a graphical user interface for GSAD, J. Appl. Cryst. 34, 210-21 (2001)). Microstructures of the ceramic samples were observed by using scanning electron microscopy (SEM), equipped with energy dispersive X-ray spectroscopy (EDS) (JSM-6335F, JEOL Japan Electronics Co., Ltd., Kyoto, Japan) at 30 kV. The morphology, microstructures and polar nanodomain regions

(PNRs) were observed using a high-resolution transmission electron microscope (HRTEM, Tecnai G2 F20 S-Twin, FEI, Hillsboro, OR, USA), acceleration voltages 200 kV, spot size 2.

2.3.2. Measurement of Specific Heat Capacity

The specific heat capacity of the samples was measured by using the Mettler Toledo DSC3 instrument according to the Sapphire method. The heat flow was measured directly in the temperature range of -50 – 200 °C such that the specific heat capacity can be given by

$$C_{p,sample} = \frac{\Phi_{sam}}{\Phi_{sap}} \frac{m_{sap}}{m_{sam}} C_{p,sap} \quad (1)$$

where $C_{p,sam}$ and $C_{p,sap}$, $\Phi_{p,sam}$ and $\Phi_{p,sap}$, m_{sam} and m_{sap} , are the specific heat (J/K·g), heat flow ($W \cdot g^{-1}$), and mass of the sintered KN-BT(9/1) bulk sample at 1050 °C and standard sapphire as reference, respectively.

2.3.3. Characterization of Dielectric and Ferroelectric Properties

To measure dielectric and ferroelectric properties of the ceramics, two sides of the disc samples were coated with Ag paste fired at 600 °C for 30 min as electrodes. Temperature-dependent dielectric characteristics were measured over 1–100 kHz by using a dielectric analyzer (TZDM-RT-800, Harbin Julang Technology Co., Ltd., Harbin, China) over -20 – 500 °C, at a rate of $1 \text{ K} \cdot \text{min}^{-1}$. Ferroelectric hysteresis (P-E) loops were recorded by using a modified Sawyer–Tower circuit method operated at a frequency of 10 Hz, over the temperature range from RT to 52 °C using the power supply Trek Model 610C.

2.3.4. Measurement of Electrocaloric Effect

Direct ECE measurement was carried out in this study. To directly measure the ECE signals, a pulsed electric field was applied to the sample with a thermocouple (Precision Fine Wire Thermocouple, Omega Engineering, Inc., Norwalk, CT, USA) attached directly to record the temperature variation as shown in Figure 1.

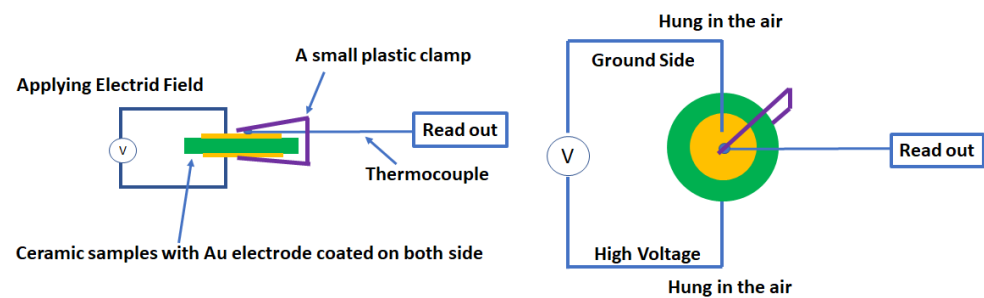


Figure 1. Schematic diagram of the electrocaloric effect measurement setup.

For measurement, the sample was hung in air through two wires to avoid any heat dissipations. The thermocouple that directly touched one surface of the sample (ground side) was connected to an oscilloscope (Teledyne LeCroy WaveSurfer 3024 Oscilloscope 200 MHz) to record the temperature, power supply: Trek Model 610C. The measurement was carried out by (i) manually applying an electric field to the sample with a positive peak appearing on the oscilloscope, (ii) waiting for the heat peak to completely pass and temperature curve to become constant, then manually removing the electric field, and (iii) showing a cooling peak. No constant pulse wide of the electric field was set. Based on the dimension of the samples, the period was about 2 s. The final cooling performance was obtained by calculating the temperature difference between the initial temperature and maximum value of the cooling peak. The precision and validity of thermocouple were checked as follows. Firstly, a heat plate with a known temperature, which was confirmed by using another infrared (IR) thermometer, was used to check the precision of the thermocouple, where the temperature read from the thermocouple should be in perfect

agreement with that read from the IR thermometer. Secondly, before the ECE of the ceramic samples was calculated, a Teflon plate with the same Au electrode coated on each side was used to check the validity. As shown in the schematic diagram, a Teflon plate was used to replace the ceramic samples, and a similar electric field was applied. No temperature changes can be read from the thermocouple. Therefore, the observed temperature changes should be the real temperature changes of ceramics.

3. Results and Discussion

3.1. Phase Composition and Microstructure of the Bimodal Structured Ceramics

Figure 2a shows XRD patterns of the commercial-grade nano-sized BaTiO_3 powder, micron-sized KNbO_3 powder (calcined at 640°C), the micron-sized KN-BT(9/1) filler powder and the nano-sized KN-BT(9/1) matrix powder calcined at 900°C respectively, together with the bimodal structured KN-BT(9/1) ceramics sintered at 1050°C using the IAGG method. The TEM (transmission electron microscope) images of the filler and matrix of KN-BT(9/1) powders calcined at 900°C are shown in Figure 2b,c.

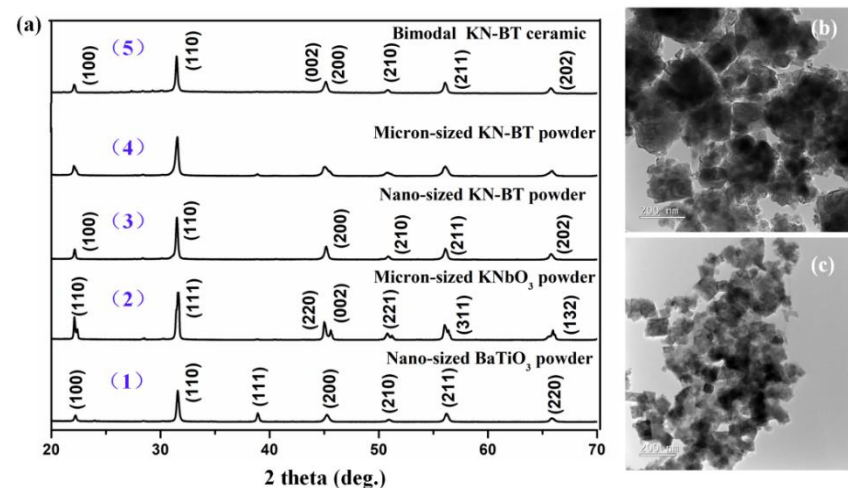


Figure 2. (a) XRD patterns of the (1–4) powders: (1) the commercial nano-sized BaTiO_3 , (2) micron-sized KNbO_3 , (3) nano-sized KN-BT(9/1) matrix powders, and (4) micron-sized KN-BT(9/1) filler powders, including (5) XRD pattern of the bimodal structured KN-BT(9/1) bulk ceramic. (b,c) TEM images of the micron-sized filler and nano-sized matrix powders calcined at 900°C respectively.

As shown in Figure 2a, all the samples exhibit a typical perovskite structure, while the commercial nano-sized BaTiO_3 powder exhibits a cubic perovskite structure (PDF: 31-174) [15]. As is well known, for perovskite solid solutions, the orthorhombic and tetragonal structures experience different lattice distortions with respect to the cubic structure. The orthorhombic phase (O-phase) and tetragonal phase (T-phase) can be identified according to the peak splitting, with $(220)_O/(002)_O$ and $(200)_T/(002)_T$ peaks for the O-phase and T-phase, respectively. Therefore, the calcined KNbO_3 powder exhibits the O-phase due to the $(220)_O/(002)_O$ splitting with higher left peak than the right one (PDF: 32-0822) [16]. On the other hand, the (IAGG-prepared) ceramic sintered at 1050°C possesses a tetragonal phase, as evidenced by the splitting of the diffraction peaks $(200)/(002)$ located near $44\text{--}47^\circ$ (inset of Figure S2a), which is in agreement with the phase transition diagram of the KN-BT system [11]. Moreover, the Rietveld refinement of the XRD pattern is shown in Figure S2b, including Figure S2c showing the corresponding crystal structure information using the Rietveld method respectively. By comparison, Figure S3a,b shows the Rietveld refinement of the parent XRD patterns, i.e., micron-sized pure KNbO_3 powders calcined at 640°C , and commercial-grade nano-sized pure BaTiO_3 powders, including the corresponding Rietveld refinement information in Figure S3c,d respectively.

As observed in Figure 2b,c, the micron-sized KN-BT(9/1) powder, as the filler, consists of the irregular crystalline particles with grain sizes of about 200–500 nm, while the nano-

sized KN-BT(9/1) powders, as the matrix, are characterized by uniform rectangle crystalline particles with an average grain size of about 100 nm.

Additionally, Figure S5 shows XRD patterns of the KN-BT(9/1) bulk ceramics prepared by using the conventional ceramic processing (Figure S1a), the sol-gel technique (Figure S1b) and IAGG method sintering at 1050 °C. All the samples exhibit the single-phase perovskite structure.

Figure 3 shows the SEM images and grain size distribution profiles of the KN-BT(9/1) ceramics fabricated using the IAGG method. As shown in Figure 3c,d, the average grain size and size distribution of the bimodal structure of the KN-BT(9/1) bulk ceramics sintered at 1000 and 1050 °C were evaluated by using the software equipped with the SEM equipment with both surface and cross-sectional SEM images at different magnifications. Clearly, the bimodal structure is demonstrated by the two well-separated distribution peaks. For the sample sintered at 1000 °C, only a small number of grains are larger than 1.0 µm in size, surrounded by nano-sized grains of ~0.1 µm. When the sintering temperature was increased to 1050 °C, the relatively large grains began to be exaggerated and elongated. Eventually, ultra-large grains with sizes of ~10–50 µm were formed. Therefore, our IAGG method is an effective way to develop bimodal grain-size distribution, with a small number of coarse grains uniformly distributed in the fine-grained matrix.

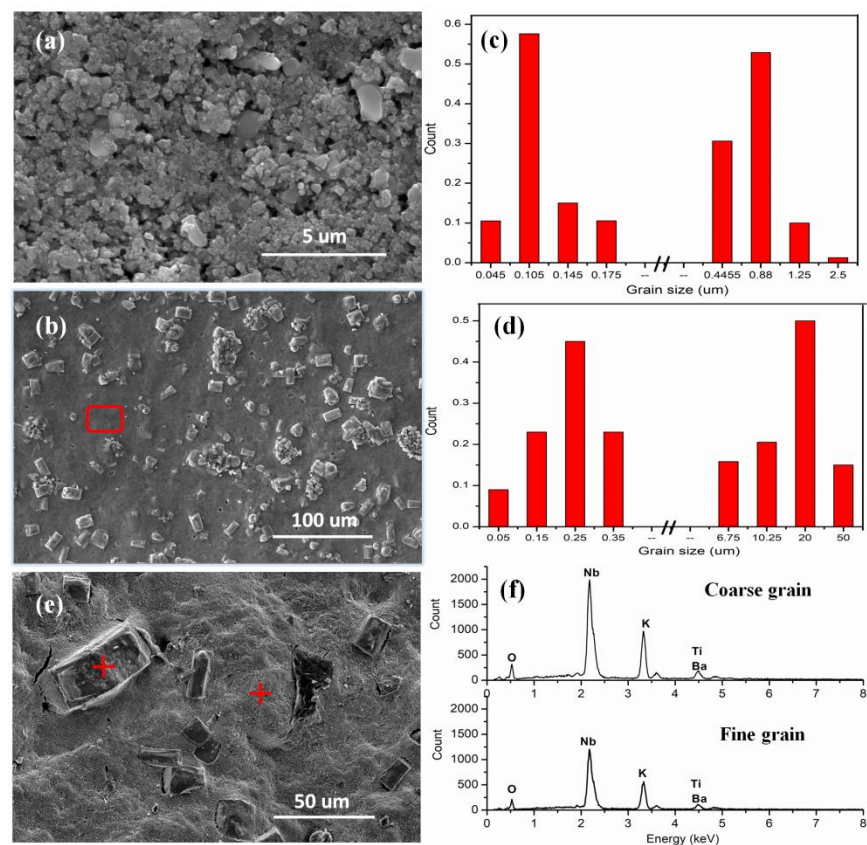


Figure 3. SEM images of the KN-BT(9/1) bulk ceramics sintered at (a) 1000 °C and (b) 1050 °C, together with (c,d) corresponding grain size distribution profiles. (e) Cross-sectional SEM image of the KN-BT(9/1) bulk ceramic sintered at 1050 °C, with (f) its corresponding EDS results, marks indicating the selected coarse and fine grains.

Here, it is very important to ensure the composition homogeneity in the coarse and fine grains. To demonstrate this, Figure 3e shows the cross-sectional surface image with high amplification. The EDS spectra of the coarse and fine grains are plotted in Figure 3f, and the automated element identification for the EDS spectra evaluation is shown in Figure S6 respectively. Indeed, the stoichiometry of the large grains is very close to that

of the fine-sized grains within the measuring uncertainties. Therefore, it is confirmed that the IAGG method is powerful for obtaining such a bimodal structure while maintaining composition homogeneity over the whole samples. In other words, the IAGG method did not trigger the uneven distribution of K^+ and Nb^{5+} in the two types of grains.

Figure 4 shows HRTEM images and the corresponding SAED (selected area electron diffraction) patterns of the coarse and fine grains. As shown in Figure 4b,c,e,f, on the one hand, the almost identical lattice planes demonstrated homogenous structure of the samples. On the other hand, the indexed KN-BT(9/1) grains exhibit the characteristic T-phase structure (PDF #71-0945). Therefore, it is concluded that the bimodal structured KN-BT(9/1) bulk ceramics have a typical T-phase as mentioned above.

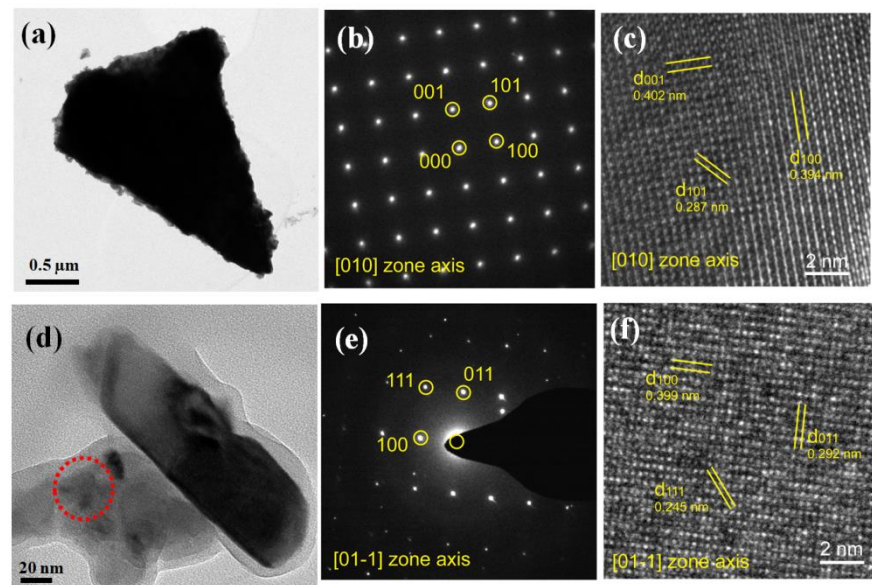


Figure 4. HRTEM images and SAED patterns of the coarse grain (a–c) and small grain (d–f). The bimodal structured KN-BT(9/1) bulk ceramic sintered at 1050 °C was selected for the analysis. Notes: the lattice planes 001, 101, 100 in [010] zone axis respectively in (b); as well as the lattice planes 111, 011, 100 in [01-1] zone axis respectively in (e).

For comparison, surface morphologies of the KN-BT(9/1) bulk ceramics fabricated using the conventional ceramic processing and sol-gel technique are shown in Figure S7a,b, together with the corresponding processing grain size distribution profiles (c,d). As expected, these two KN-BT(9/1) bulk samples with unimodal structures, with grain sizes of about 250 nm and 300–400 nm, respectively. No abnormal grain growth (AGG) phenomena are observed in the samples sintered at 1050 °C.

Grain growth behavior of the KN-BT(9/1) ceramics prepared by using the IAGG method can be understood with the explanation of Kingery and Kanget et al. [17,18]. Due to the difference in free-energy across a curved grain boundary, the irregular micron-sized KN-BT(9/1) filler powders with large curvature, underwent exaggerated growth, acting as a “seed” to consume the neighboring nano-sized ones in the matrix. Therefore, in a given polycrystalline system, the grain growth behavior is governed by the maximum driving force (Δg_{max}) relative to the critical driving force (Δg_c), showing the mixed controlling growth behavior. Although the grain size could be increased by sintering at very high temperatures or for very longer times in theory, no grain growth with specific morphologies and crystal orientations of large grains occur when Δg_{max} is smaller than Δg_c . Therefore, our IAGG method in this study is an effective way to develop ceramics with extraordinarily oriented large grains at relatively low sintering temperatures when using the solid-state reaction process. It seems that the filler grains are “cloned”, while the gel matrix is just like a “nutrient source or reservoir” to breed the fillers to grow. This method is simple, reproducible and low cost, which can be easily extended many other ferroelectric perovskite materials.

3.2. Dielectric and Ferroelectric Properties

Figure 5 shows dielectric properties dependent of the temperature ($\epsilon_r(T)$) at different frequencies, and the microstructure of the KN-BT(9/1) bulk ceramics sintered at 1050 °C. As shown in Figure 5a, all the $\epsilon_r(T)$ curves exhibit a broad peak centered at about $-20\sim 100$ °C, indicating that diffused phase transition is present in the KN-BT(9/1) bulk ceramic [11,19]. At RT, the relative permittivity (ϵ_r) and loss tangent are about 792 and 0.067 at 1 kHz, respectively. The diffused behavior is further confirmed by the dielectric loss curves.

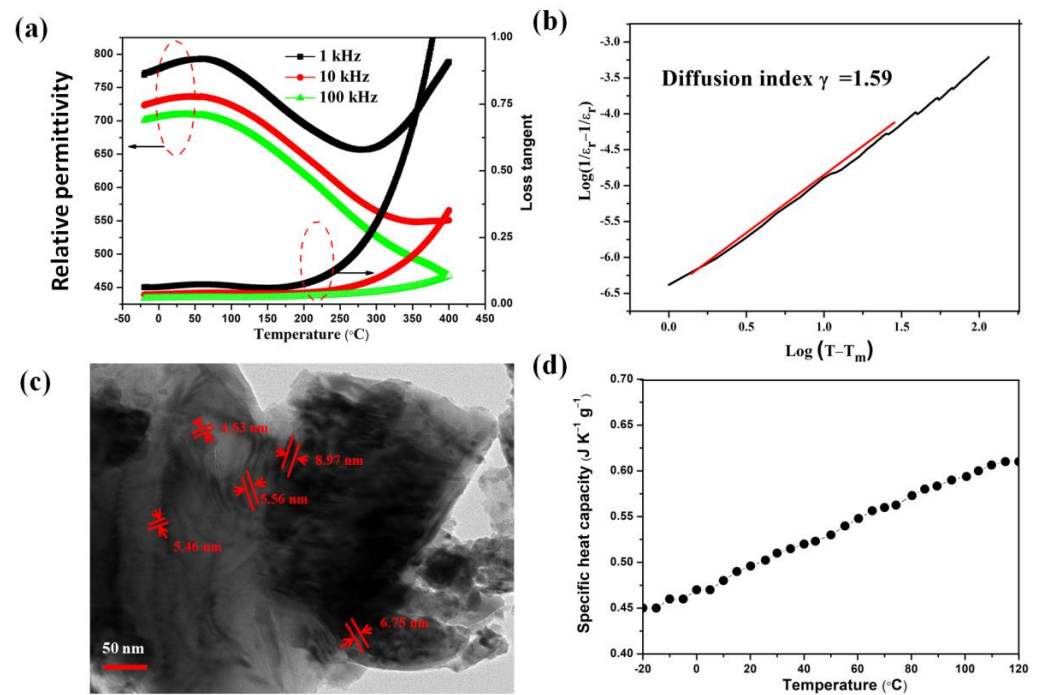


Figure 5. (a) Dielectric properties versus temperature at three selected frequencies (1 kHz, 10 kHz and 100 kHz). (b) Plot of $\log(\frac{1}{\epsilon_r} - \frac{1}{\epsilon_m})$ as a function of $\log(T - T_m)$ at 100 kHz. (c) TEM image of polar nanodomain regions (PNRs) in the sample. (d) Measured specific heat capacity of the KN-BT(9/1) ceramics. Note that the bimodal structured KN-BT(9/1) bulk ceramic sintered at 1050 °C using IAGG method was selected for the analysis.

For relaxor ferroelectrics, the reciprocal of relative permittivity as a function of temperature, follows the Uchino and Nomura function, a modified Curie–Weiss law, which is expressed as [20]

$$\frac{1}{\epsilon_r} - \frac{1}{\epsilon_m} = \frac{(T - T_m)^\gamma}{C} \quad (2)$$

where C is the Curie constant and γ is the diffusion coefficient ranging from 1 (an ideal normal ferroelectric) to 2 (an ideal relaxor ferroelectric); ϵ_m and T_m are the maximum relative permittivity and corresponding temperature at a fixed frequency, respectively. The slope of the fitting curves is used to determine the γ value in the Figure 5b. The value is $\gamma = 1.59$ at 100 kHz, confirming the relaxor-like ferroelectric behavior of the KN-BT(9/1) bulk sample.

The ferroelectric nanodomains were observed through HRTEM images, as shown in Figure 5c, displaying grains with sizes of 2–10 nm randomly in the nondomain matrix. The presence of the PNRs provides strong evidence of the diffusion phase during the phase transition in the KN-BT(9/1) bulk sample. The diffused phase transition can be ascribed to the partial breaking of the ferroelectric long-range ordering by the coupled substitutions of Ba²⁺ and Ti⁴⁺ ions for K⁺ and Nb⁵⁺ ions with different sizes and charges, respectively, due to the simultaneous occupation of the six-coordination site by Ti⁴⁺ and Nb⁵⁺ [11,21,22].

Moreover, it is believed that the presence of the fine-size grains in the bimodal structured sample is responsible for additional decrease in the T_m [23].

As illustrated in Figure 5d, no obvious anomaly is observed in the specific heat capacity. The specific heat capacity value is increased with increasing temperature, with a room temperature value of $0.50 \text{ J}\cdot\text{K}^{-1}\cdot\text{g}^{-1}$. As shown in Figure S8, a weak anomaly is present on the heat capacity curve, which is similar to the observation of Pb-free relaxor $\text{Ba}(\text{Ti}_{0.65}\text{Zr}_{0.35})\text{O}_3$ ceramics [24].

Figure 6a shows P-E hysteresis loops of the KN-BT(9/1) bulk sample sintered at 1050°C measured at RT and 52°C at 10 Hz. Figure 6b illustrates P-E curves measured at different electrical fields, while the curve of the remanent polarization versus the electric field at RT is shown as the inset in Figure 6b.

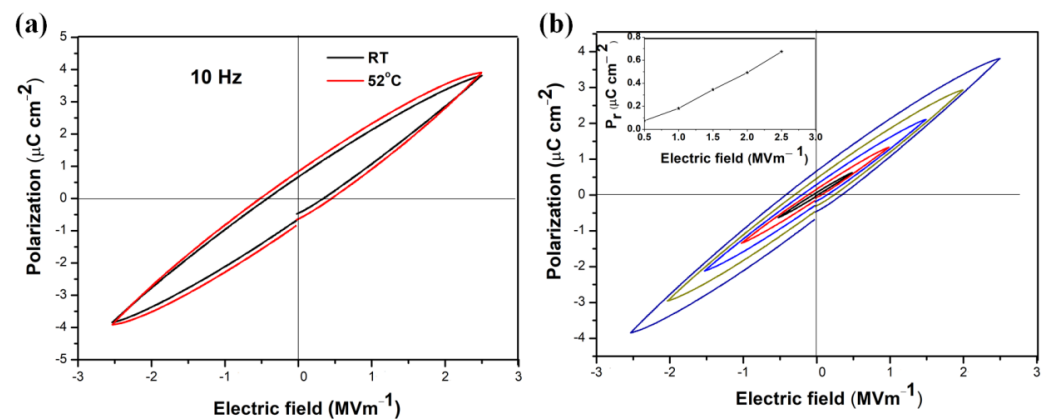


Figure 6. (a) P-E loops measured at RT and 52°C at 10 Hz. (b) P-E loops measured at different electric fields at RT, with the inset showing the remanent polarization (P_r) versus electric field. Note that the bimodal structured KN-BT(9/1) bulk ceramic sintered at 1050°C using the IAGG method was selected for the analysis.

The sample has a ferroelectric nature, whereas the slim P-E hysteresis loops suggest that the ceramics have low hysteresis losses. The P-E loops at RT and 52°C were nearly the same, indicating that the presence of ferroelectricity in nature can be retained over a relatively broad temperature range. Additionally, as seen in Figure 6b, the P-E loop is electric field dependent, with the remanent polarization to be increased almost linearly with the increasing electric field. At $2.5 \text{ MV}\cdot\text{m}^{-1}$ and RT, the values of the P_r and the coercive field (E_C) are $0.675 \mu\text{C}\cdot\text{cm}^{-2}$ and $0.23 \text{ MV}\cdot\text{m}^{-1}$, respectively. By comparison, the P-E loops of the KN-BT(9/1) bulk samples sintered at 1050°C using the conventional ceramic processing and sol-gel technique are shown in Figure S9. Obviously, lossy hysteresis loops are present, indicating higher conductive behavior in a unimodal structure. Therefore, our bimodal structured bulk ceramic displays a relatively good ferroelectric property. It can be inferred that the extra-large grains ensure the ferroelectricity, while the fine grains ensure high density to suppress the tunneling current [25].

3.3. Electrocaloric Effect

ECE adiabatic ΔT refers to the temperature drop induced after removing the electric field. The typical thickness of the KN-BT(9/1) bulk sample used in the ECE measurement was 0.264 mm with an *electrode diameter* of 6 mm . The specific isothermal entropy change, ΔS , is calculated with $\Delta S = c \Delta T/T$, where c is the specific heat of the ceramic sample [26]. Figure 7a shows the directly recorded ECE signal of the bulk sample at RT at $1 \text{ MV}\cdot\text{m}^{-1}$, where the temperature is demonstrated to rise and drop as the field is applied and removed. The ΔT and ΔS at RT at different electric fields are presented in Figure 7b. The ratios of $\left| \frac{\Delta T}{\Delta E} \right|$ and $\Delta S/\Delta E$ (or $\Delta Q/\Delta E$, where $\Delta Q = T\Delta S$) are used to express the electrocaloric coefficients (ECE strengths). It is found that the KN-BT(9/1) ceramics have high ECE at $E = 1 \text{ MV}\cdot\text{m}^{-1}$, corresponding to $\Delta T = -1.5 \text{ K}$ and $\Delta S = 2.48 \text{ J}\cdot\text{kg}^{-1}\cdot\text{K}^{-1}$. Accordingly,

$\left| \frac{\Delta T}{\Delta E} \right| = 1.50 \times 10^{-6} \text{ K} \cdot \text{m} \cdot \text{V}^{-1}$ and $\Delta S / \Delta E = 2.48 \times 10^{-6} \text{ J} \cdot \text{m} \cdot \text{kg}^{-1} \cdot \text{K}^{-1} \cdot \text{V}^{-1}$ were obtained at RT. As discussed above, the strongly widened phase transition temperature near RT is responsible for the giant ECE response over a relatively broad temperature range [4,5].

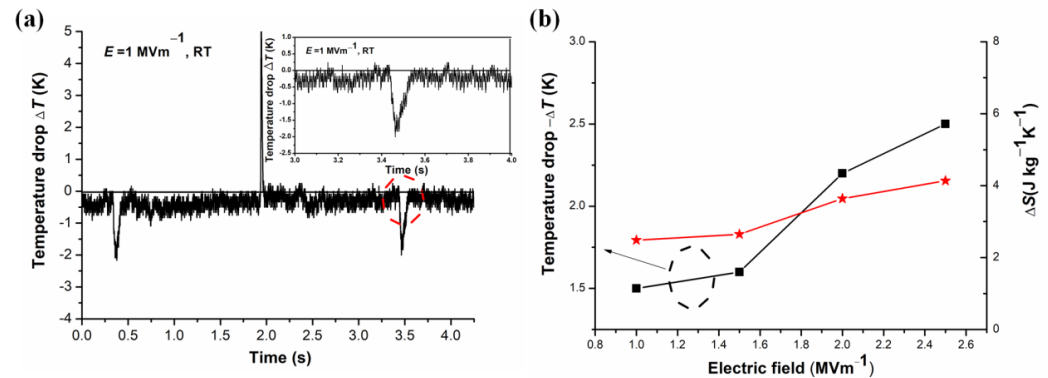


Figure 7. (a) Directly recorded ECE signal for the KN-BT(9/1) sample as the electric field was switched on and off. Solid line is drawn to show the ambient temperature. The amplified temperature drop is shown as the inset. (b) ECE-induced adiabatic temperature drop (ΔT) and isothermal entropy change (ΔS) as a function of electric field (E) at RT. The dash line is drawn to guide eyes. Note that the bimodal structured KN-BT(9/1) bulk ceramic sintered at 1050 °C using IAGG method was selected for the analysis. Error: within the noise range, it is about ± 0.2 °C.

Additionally, as shown in Table 1, compared with the ferroelectric ceramics reported in refs. [8,9,25–31], our bimodal structured KN-BT(9/1) bulk ceramics shows a fairly high ECE coefficient (strength), which is close to the ECE of single crystal BaTiO₃ at 10 °C. Besides the diffused phase transition temperature near RT, the coarse grains (10–50 μm) in the bimodal structure should enhance the dielectric and ferroelectric properties of the sample, resulting in high ECE strength at relatively low electric fields [23]. At the same time, the finer grains derived from the matrix play a crucial role in forming a dense microstructure and inhomogeneous dielectric properties, leading to high entropy [3].

Table 1. ECEs of different ferroelectric ceramics with operating temperature near RT.

Material	Form	T (°C)	ΔT (K)	E (MV m ⁻¹)	$\left \frac{\Delta T}{\Delta E} \right $ (10 ⁻⁶ Km V ⁻¹)	$\Delta S / \Delta E$ (10 ⁻⁶ Jm kg ⁻¹ K ⁻¹ V ⁻¹)	Method	Reference
KN-BT(9/1)	Ceramic	23	1.5	1	1.50	2.48	Direct	This work
Ba(ZrxTi1-x)O3	Ceramic	38	1.1	2.1	0.52	0.93	Direct	[26]
Bi0.5Na0.5TiO3-based	Ceramic	23	0.45	3	-	-	Direct	[9]
Ba0.65Sr0.35TiO3	Ceramic	23	0.4	2	0.21	-	Indirect	[27]
(Pb, La, Ba)(Zr, Sn, Ti)O3	Ceramic	30	0.25	2.2	0.11	-	Direct	[28]
PZT-5	Ceramic	30	0.15	2.8	0.05	-	Direct	[29]
(Ba, Ca)(Zr, Ti)O3	Ceramic	60	0.3	2.0	0.15	-	Indirect	[30]
0.9PMN-0.1PT	Ceramic	25	0.63	2.8	0.23	-	Direct	[25]
BaTiO3	Single crystal	10	1.4	1	1.4	-	Direct	[31]
0.9PMN-0.1PT	Single crystal	50	1.0	4.00	0.25	-	Indirect	[8]

However, the unimodal structured KN-BT(9/1) made by using the conventional ceramic processing and sol-gel technique cannot be used to measure the ECEs, apparently, the novel bimodal structured KN-BT(9/1) bulk ceramics by the IAGG method can overcome the shortage of the unimodal structured samples. Additionally, the preparation of the bimodal structured KN-BT(9/1) ceramics using the IAGG method is highly compatible with the conventional ceramic process, giving them potential as micro-refrigerators to be used for cooling the microelectronic devices near RT.

4. Conclusions

Bimodal structured KN-BT(9/1) bulk ceramics with a tetragonal phase at RT and a diffused phase transition were prepared successfully by using the IAGG method at a

relatively low sintering temperature of 1050 °C. In this bimodal structure, the exaggeratedly large grains were evolved from the micron-sized KN-BT(9/1) filler powders, while the fine grains were originated from the KN-BT(9/1) sol precursor matrix. As compared with the unimodal structured counterpart, the bimodal structured KN-BT(9/1) bulk ceramics display a high electrocaloric performance, giving a large ECE-induced adiabatic temperature drop of 1.5 K and a large EC coefficient of $2.48 \times 10^{-6} \text{ J}\cdot\text{m}\cdot\text{kg}^{-1}\cdot\text{K}^{-1}\cdot\text{V}^{-1}$ at RT, which is advantageous to the design of cooling devices. It is believed that the coarse grains engender the high ferroelectricity and ECE strengths, while the fine grains are responsible for the decreased maximum temperature, and the enhanced density. Our IAGG method is simple, reproducible and cost effective, which can be easily extended to other ferroelectric perovskite materials.

Supplementary Materials: The following supporting information can be downloaded at: <https://www.mdpi.com/article/10.3390/nano12152674/s1>, Figure S1: Synthesis routes using (a) the conventional ceramic processing, (b) Sol-gel technique using the modified Pechini method, and (c) The induced abnormal grain growth method (IAGG). Figure S2: (a) XRD patterns of the bimodal structure KN-BT(9/1) bulk ceramics sintered at 1050 °C using IAGG method. (b) The Rietveld refinement of XRD pattern using the GSAS refinement software, including (c) corresponding crystal structure information through the Rietveld method Inset shows Zoom-in view of 44–47°. Figure S3: The Rietveld refinement of the parent XRD patterns: (a) micron-sized KNbO₃ powders calcined at 640 °C, (b) commercial-grade nano-sized BaTiO₃ powders. (c,d) Corresponding crystal structure information through the Rietveld method using the GSAS refinement software respectively. Figure S4: (a) XRD patterns of the commercial nano-sized BaTiO₃ (BT) powder, micron-sized KNbO₃ (KN) and KN-BT(9/1) filler powders using the conventional ceramic processing, together with a bimodal structure KN-BT(9/1) bulk ceramics sintered at 1050 °C using IAGG method. (b) Zoom-in view of 44–47°. The dash line and arrow are drawn to guide eyes. Figure S5: XRD patterns of the KN-BT(9/1) bulk ceramics prepared by using the conventional ceramic processing (i.e., solid-state reaction), sol-gel technique and IAGG method at 1050 °C respectively. Figure S6: The automated element identification for EDS spectra evaluation for (a) Coarse grain. (b) Fine grain respectively. Figure S7: SEM images of the KN-BT(9/1) ceramics prepared at 1050 °C by using (a) sol-gel technique and (b) the conventional solid-state processing, (c) and (d) are corresponding to (a) and (b) respectively. Figure S8: (a,b) The measured specific heat capacity as a function of temperature, together with the enlarge segment between 10–50 °C. (c) The loss tangent dependent of the temperature at different frequency. The red dash circle was drawn to guide eyes. Figure S9: Room-temperature P-E loops of the KN-BT(9/1) ceramics sintered at 1050 °C using (a) the conventional ceramic processing, (b) the sol-gel technique. The corresponding enlarged segments of loops are shown in the Figure S9c and Figure S9d respectively. The red dash circles were drawn to guide eyes.

Author Contributions: Conceptualization, investigation, and writing—original draft preparation, H.Z.; funding acquisition, J.G.; methodology, L.L. and B.P.; writing—review and editing, K.W.K. and L.-B.K.; methodology, S.-G.L.; software, F.H. All authors have read and agreed to the published version of the manuscript.

Funding: This work was supported by the National Natural Science Foundation of China (Grant No. 11974304).

Institutional Review Board Statement: Not applicable.

Informed Consent Statement: Not applicable.

Data Availability Statement: The data presented in this study are available in this article and supplementary file.

Acknowledgments: We thank Xin Chen, Department of Material Science and Engineering, Material Research Institute, The Pennsylvania State University, for the measurement and analysis of the ECE data.

Conflicts of Interest: The authors declare no conflict of interest.

References

1. Neese, B.; Chu, B.; Lu, S.G.; Wang, Y.; Furman, E.; Zhang, Q.M. Large electrocaloric effect in ferroelectric polymers near room temperature. *Science* **2008**, *321*, 821–823. [[CrossRef](#)]
2. Mischenko, A.S.; Zhang, Q.; Scott, J.F.; Whatmore, R.W.; Mathur, N.D. Giant electrocaloric effect in thin-film $\text{PbZr}_{0.95}\text{Ti}_{0.05}\text{O}_3$. *Science* **2006**, *311*, 1270–1271. [[CrossRef](#)]
3. Qian, X.S.; Han, D.L.; Zheng, L.R.; Chen, J.; Tyagi, M.; Li, Q.; Du, F.H.; Zheng, S.Y.; Huang, X.Y.; Zhang, S.H.; et al. High-entropy polymer produces a giant electrocaloric effect at low fields. *Nature* **2021**, *600*, 664–669. [[CrossRef](#)]
4. Shi, J.; Han, D.; Li, Z.; Yang, L.; Lu, S.-G.; Zhong, Z.; Chen, J.; Zhang, Q.M.; Qian, X. Electrocaloric cooling materials and devices for zero-global-warming-potential, high-efficiency refrigeration. *Joule* **2019**, *3*, 1200–1225. [[CrossRef](#)]
5. Barman, A.; Kar-Narayan, S.; Mukherjee, D. Caloric effects in perovskite oxides. *Adv. Mater. Interfaces* **2019**, *6*, 1900291. [[CrossRef](#)]
6. Gu, H.; Qian, X.; Li, X.; Craven, B.; Zhu, W.; Cheng, A.; Yao, S.C.; Zhang, Q.M. A chip scale electrocaloric effect based cooling device. *Appl. Phys. Lett.* **2013**, *102*, 122904. [[CrossRef](#)]
7. Tuttle, B.A.; Payne, D.A. The effects of microstructure on the electrocaloric properties of $\text{Pb}(\text{Zr},\text{Sn},\text{Ti})\text{O}_3$ ceramics. *Ferroelectrics* **1981**, *37*, 603–606. [[CrossRef](#)]
8. Luo, L.; Chen, H.; Zhu, Y.; Li, W.; Luo, H.; Zhang, Y. Pyroelectric and electrocaloric effect of $\langle 111 \rangle$ -oriented 0.9PMN–0.1PT single crystal. *J. Alloys Compd.* **2011**, *509*, 8149–8152. [[CrossRef](#)]
9. Li, G.H.; Shi, C.; Zhu, K.; Ge, G.L.; Yan, F.; Lin, J.F.; Shi, Y.J.; Shen, B.; Zhai, J.W. Achieving synergistic electromechanical and electrocaloric responses by local structural evolution in lead-free BNT-based relaxor ferroelectrics. *Chem. Eng. J.* **2022**, *431*, 133386. [[CrossRef](#)]
10. Lines, M.E.; Glass, A.M. *Principles and Applications of Ferroelectrics and Related Materials*; Oxford University Press: New York, NY, USA, 1977; Volume 66.
11. Bratton, R.J.; Tien, T.Y. Phase transitions in the system BaTiO_3 - KNbO_3 . *J. Am. Ceram. Soc.* **1967**, *50*, 90–93. [[CrossRef](#)]
12. Birks, E.; Duce, M.; Sternberg, A. High electrocaloric effect in ferroelectrics. *Ferroelectrics* **2010**, *400*, 336–343. [[CrossRef](#)]
13. Pribosic, I.; Makovec, D.; Drogenik, M. Chemical synthesis of KNbO_3 and KNbO_3 - BaTiO_3 ceramics. *J. Eur. Ceram. Soc.* **2005**, *25*, 2713–2717. [[CrossRef](#)]
14. Zhang, H.F.; Chen, X.; Gao, J.; Lam, K.H.; Liang, S.D.; Fei, L.F.; Mak, C.L.; Chen, J.F. The fabrication and electrocaloric effect of bimodal-grain structure $(\text{Ba}_{0.60}\text{Sr}_{0.40})\text{TiO}_3$ using the induced abnormal grain growth method. *IOP Conf. Ser. Mater. Sci. Eng.* **2019**, *678*, 012138. [[CrossRef](#)]
15. Hreniak, D.; Streck, W.; Amami, J.; Guyot, Y.; Boulon, G.; Goutaudier, C.; Pazik, R. The size-effect on luminescence properties of $\text{BaTiO}_3:\text{Eu}^{3+}$ nanocrystallites prepared by the sol-gel method. *J. Alloys Compd.* **2004**, *380*, 348–351. [[CrossRef](#)]
16. Kakimoto, K.; Masuda, I.; Ohsato, H. Ferroelectricity and solid-solution structure of KNbO_3 ceramics doped with La and Fe. *Key Eng. Mater.* **2004**, *269*, 7–10. [[CrossRef](#)]
17. Kingery, W.D.; Bowen, H.K.; Uhlmann, D.R. *Introduction to Ceramics*; John Wiley & Sons: Hoboken, NJ, USA, 1976; Volume 17.
18. Kang, S.L.; Ko, S.Y.; Moon, S.Y. Mixed control of boundary migration and the principle of microstructural evolution. *J. Ceram. Soc. Jpn.* **2016**, *124*, 259–267. [[CrossRef](#)]
19. Ravez, J.; Simon, A. Relaxor ferroelectricity in ceramics with composition $\text{Ba}_{1-x}\text{Kx}(\text{Ti}_{1-x}\text{Nb}_x)\text{O}_3$. *Mater. Lett.* **1998**, *36*, 81–84. [[CrossRef](#)]
20. Uchino, K.; Nomura, S. Critical exponents of the dielectric constants in diffused-phase-transition crystals. *Ferroelectr. Lett.* **1982**, *44*, 55–61. [[CrossRef](#)]
21. Zheng, S.; Odendo, E.; Liu, L.; Shi, D.; Huang, Y.; Fan, L.; Chen, J.; Fang, L.; Elouadi, B. Electrostrictive and Relaxor Ferroelectric Behavior in BiAlO_3 -Modified BaTiO_3 Lead-Free Ceramics. *J. Appl. Phys.* **2013**, *113*, 094102. [[CrossRef](#)]
22. Liu, L.; Knapp, M.; Ehrenberg, H.; Fang, L.; Fan, H.; Schmitt, L.A.; Fuess, H.; Hoelzel, M.; Dammak, H.; Thi, M.P.; et al. Average vs. Local Structure and Composition-Property Phase Diagram of $\text{K}_{0.5}\text{Na}_{0.5}\text{NbO}_3$ - $\text{Bi}_{\frac{1}{2}}\text{Na}_{\frac{1}{2}}\text{TiO}_3$ System. *J. Eur. Ceram. Soc.* **2017**, *37*, 1387–1399. [[CrossRef](#)]
23. Lu, S.G.; Liu, H.L.; Han, Y.; Zhang, L.Y.; Yao, X. Phase-transition of nanophase ferroelectric PbTiO_3 ultrafine powders. *Ferroelectr. Lett.* **1994**, *18*, 115–120. [[CrossRef](#)]
24. Nagasawa, M.; Kawaji, H.; Tojo, T.; Atake, T. Absence of the heat capacity anomaly in the Pb-free relaxor $\text{BaTi}_{0.65}\text{Zr}_{0.35}\text{O}_3$. *Phys. Rev. B* **2006**, *74*, 132101. [[CrossRef](#)]
25. Vrabelj, M.; Ursic, H.; Kutnjak, Z.; Rozic, B.; Drnovsek, S.; Bencan, A.; Bobnar, V.; Fulanovic, L.; Malic, B. Large electrocaloric effect in grain-size-engineered $0.9\text{Pb}(\text{Mg}_{1/3}\text{Nb}_{2/3})\text{O}_3$ - 0.1PbTiO_3 . *J. Eur. Ceram. Soc.* **2016**, *36*, 75–80. [[CrossRef](#)]
26. Qian, X.S.; Ye, H.J.; Zhang, Y.T.; Gu, H.M.; Li, X.Y.; Randall, C.A.; Zhang, Q.M. Giant electrocaloric response over a broad temperature range in modified BaTiO_3 ceramics. *Adv. Funct. Mater.* **2014**, *24*, 1300–1305. [[CrossRef](#)]
27. Bai, Y.; Han, X.; Ding, K.; Qiao, L.J. Combined effects of diffuse phase transition and microstructure on the electrocaloric effect in $\text{Ba}_{1-x}\text{Sr}_x\text{TiO}_3$ ceramics. *Appl. Phys. Lett.* **2013**, *103*, 162902.
28. Wang, J.; Yang, T.; Chen, S.; Li, G.; Yao, X. Characteristics and dielectric properties of $(\text{Pb}_{0.97-x}\text{La}_{0.02}\text{Ba}_x)(\text{Zr}_{0.72}\text{Sn}_{0.22}\text{Ti}_{0.06})\text{O}_3$ ceramics. *J. Alloys Compd.* **2012**, *539*, 280–283.
29. Wang, J.F.; Yang, T.Q.; Wei, K.; Yao, X. Temperature-electric field hysteresis loop of electrocaloric effect in ferroelectricity-direct measurement and analysis of electrocaloric effect. *Appl. Phys. Lett.* **2013**, *102*, 152907. [[CrossRef](#)]

30. Bai, Y.; Han, X.; Qiao, L.J. Optimized electrocaloric refrigeration capacity in lead-free $(1-x)\text{BaZr}_{0.2}\text{Ti}_{0.8}\text{O}_{3-x}\text{Ba}_{0.7}\text{Ca}_{0.3}\text{TiO}_3$ ceramics. *Appl. Phys. Lett.* **2013**, *102*, 252904.
31. Bai, Y.; Ding, K.; Zheng, G.P.; Shi, S.Q.; Cao, J.L.; Qiao, L.J. The electrocaloric effect around the orthorhombic-tetragonal first-order phase transition in BaTiO_3 . *AIP Adv.* **2012**, *2*, 022162.